Feasibility Study on Qinghai Lake Boundary Detection Using CYGNSS Raw IF Data

Yun Zhang, Ziyu Yan, Shuhu Yang, Wanting Meng, Yanling Han, and Zhonghua Hong

***Abstract*—Qinghai Lake, the largest inland saltwater lake in China, is an important water body that maintains the ecological security of the northeastern Tibetan Plateau. Global navigation satellite system reflectometry technology (GNSS-R) is rarely used in lake detection, especially in lake boundary detection under the circumstances of spaceborne. This article attempts to implement lake boundary detection using cyclone global navigation satellite system (CYGNSS) raw intermediate frequency (IF) data for the first time. First, the second-order frequency-locked loop is used to assist the third-order phase-locked loop closed-loop tracking to successfully generate higher delay resolution and Doppler resolution (67 × 51) delay Doppler maps (DDM) than CYGNSS compressed DDM (11 × 17); second, based on the principle of scattering characteristics of different reflectors of GNSS-R, and the fusion method of signal power ratio and effective area delay distance (D_{LR}), the 2018 Qinghai Lake boundary detection inversion was carried out in the lake area to explore the feasibility of achieving higher spatial resolution (0.7 km) and high-precision lake boundary detection with the raw IF data of CYGNSS. The inversion detection results are compared with the topographic distribution results of Google Earth and global land analysis and discovery, and the inversion result error is about 0.5 km, which is consistent with the theoretical spatial resolution. It proves that spaceborne GNSS-R technology and CYGNSS raw IF data have great potential in the field of lake boundary detection.**

***Index Terms*—Cyclone global navigation satellite system (CYGNSS), high resolution, power ratio (PR), raw intermediate frequency (IF) data, river detection.**

I. Introduction

As AN important carrier of surface water resources and a basic unit of water resources management, real-time monitoring of hydrological data, such as boundary, velocity, water level, and discharge of rivers, plays an important role [1]. Qinghai Lake, the largest inland saltwater lake in China, is in the northeast margin of the Qinghai–Tibet Plateau. It is a natural barrier to prevent the eastward spread of desertification in the west and an important node to maintain the ecological security in the northeast of the Qinghai–Tibet Plateau. Therefore, it is of great significance to study the boundary detection of Qinghai Lake [2].

At present, lake boundary detection mainly relies on optical remote sensing and microwave remote sensing. Optical remote sensing images provide useful information on large areas of lakes and ice sheets. Some traditional techniques, such as Sobel [3], zero-crossing [4], multiscale [5], and structured edges [6], frequently have been applied for detecting boundaries. The measurement results of the optical monitoring method are related to the composition of ground objects, and climatic conditions (such as clouds and rain), which have meter-level accuracy [7].

River monitoring methods, such as very-high-frequency ground wave radar [8], active and passive microwave radar [9], [10], and spaceborne multispectral [11], have emerged, supplementing the observation of large-scale rivers or ice sheets to a certain extent. Unlike optical sensors, spaceborne synthetic aperture radar based on microwave imaging can provide stream distribution in complex climates [12].

Global navigation satellite system reflectometry (GNSS-R) technology is a new passive remote sensing means of processing navigation satellite signals reflected by ocean and land, and the features of the target reflector surface can be extracted [13]. GNSS-R technology, which uses dual-base radar mode and uses the globally shared GNSS constellation as multisource microwave signal emission sources, has been widely used in sea surface height measurement [14], [15], sea surface wind measurement [16], [17], soil moisture detection [18], oil spillage detection [19], sea ice detection [20], and other fields.

Scholars have carried out research on the use of GNSS-R to detect inland water bodies. In literature [21] and [22], GNSS-R technology was applied to measure the water level of lakes and rivers, and the measuring accuracy of cm level and ∼0.30 m was obtained, respectively. In the application of GNSS-R lake inversion, Li et al. [23] used cyclone global navigation satellite system (CYGNSS) intermediate frequency (IF) data to measure the height of Qinghai Lake and preliminarily demonstrated the feasibility of satellite-based carrier phase measurement of inland water level. However, due to the spatial resolution (50 ms integration time: along the track ∼350 m [24]), this technology cannot be applied to small- and medium-sized rivers. In terms

Manuscript received 12 November 2023; revised 27 February 2024; accepted 20 March 2024. Date of publication 3 April 2024; date of current version 19 April 2024. This work was supported by the National Natural Science Foundation of China under Grant 42271335 and Grant 42176175. *(Corresponding author: Shuhu Yang.)*

Yun Zhang, Shuhu Yang, Yanling Han, and Zhonghua Hong are with the College of Information Technology, Shanghai Ocean University, Shanghai 201306, China, and also with the Shanghai Marine Intelligent Information and Navigation Remote Sensing Engineering Technology Research Center, Shanghai Ocean University, Shanghai 201306, China (e-mail: y-zhang@shou.edu.cn; shyang@shou.edu.cn; ylhan@shou.edu.cn; zhhong@shou.edu.cn).

Ziyu Yan is with the College of Information Technology, Shanghai Ocean University, Shanghai 201306, China, also with the Key Laboratory of Fisheries Information, Ministry of Agriculture, Shanghai 201306, China, and also with the Ocean College, Zhejiang University, Hangzhou 316021, China (e-mail: 12334037@zju.edu.cn).

Wanting Meng is with the Shanghai Spaceflight Institute of TT&C and Telecommunication, Meteorological Payload Department, Shanghai 201109, China (e-mail: wanting_meng@163.com).

Digital Object Identifier 10.1109/JSTARS.2024.3384235

of river flow detection, Warnock et al. used CYGNSS IF data to define the correlation width of time delay waveform inverts the flow of the Mississippi River and finds that associated GNSS-R width is proportional to the flow of the river, demonstrating the feasibility of spaceborne GNSS-R detecting the flow of the river [25]. In terms of velocity detection, literature [26], [27], and [28] all found that GNSS signals reflected by flow surface had a small Doppler deviation compared with direct signals, which was related to fluid velocity. All these indicate that GNSS-R technology has certain potential in river detection. However, only Level-1 (L1) data were used for lake boundary detection, and the low spatial resolution of L1 data cannot meet the higher resolution requirement [20]. In parallel, there is no research on lake boundary detection using the raw IF data of satellite-borne GNSS-R. NASA's CYGNSS constellation, launched in 2016, consists of eight small and low-cost satellites. The CYGNSS instrument records the reflected signal (called raw IF data) to produce different level data [29]. Compared with CYGNSS L1 data, using a software-defined receiver to process the raw IF data of GNSS-R can extract more potential information, mine more information about the physical characteristics of the reflective surface, and obtain tracking related results with higher resolution. The inversion results would have higher precision and higher spatiotemporal resolution [30].

Compared to spaceborne optical remote sensing (Sentinel 2) and radar remote sensing missions (Envisat, CryoSat-2, and operation ice bridge), GNSS-R technology has the advantages of easy networking, high time resolution, low cost, and not affected by weather.

In this article, CYGNSS raw IF data were used for lake boundary detection for the first time. The raw IF datasets received by CYGNSS in Qinghai Lake region in 2018 was successfully generated by using second-order frequency locking loop assisted third-order phase-locked loop closed-loop tracking method with higher dimensional resolution than the CYGNSS L1 data. Based on the scattering characteristic principle of different reflecting surfaces of GNSS-R, the fusion method of power ratio (PR) and effective area delay distance (D_{LR}) were used to distinguish lake, ice and land, and realize the boundary detection of Qinghai Lake. Finally, Google Earth was used to extract the boundary to verify the inversion results in this article.

II. Inversion Datasets

A. CYGNSS Raw IF Dataset in Qinghai Lake

Qinghai Lake is a saline–alkali lake located in the hollow area of the northeast of the Qinghai–Tibet Plateau. It is the largest saltwater lake in China. Ranging from 36°32'N to 37°15' N (about 70 km), 99°36'–100°E ∘ 47'E (about 100 km), and the altitude is ∼3200 m [31]. The orbital inclination of CYGNSS satellites is about 35°, and the satellite coverage is between 38°N and 38°S latitudes, including the Qinghai Lake Basin.

This article mainly uses the raw IF data collected near Qinghai Lake in 2018. By matching the time stamp and latitude and longitude with CYGNSS L1 data, a total of 10 mirror tracks across the lake were found. The software receiver was used to analyze these raw IF data. The data are processed to generate a delay Doppler maps (DDM) with a higher resolution than the CYGNSS L1 data as the data basis for the inversion in this article. The main information of these trajectories, including data acquisition time, CYGNSS spacecraft (SC) ID, GNSS PRN, trajectory duration, incident angle, number of DDMs, etc., combined with the article [23] gives the corresponding surface state of Qinghai Lake, and the summary information is shown in Table I.

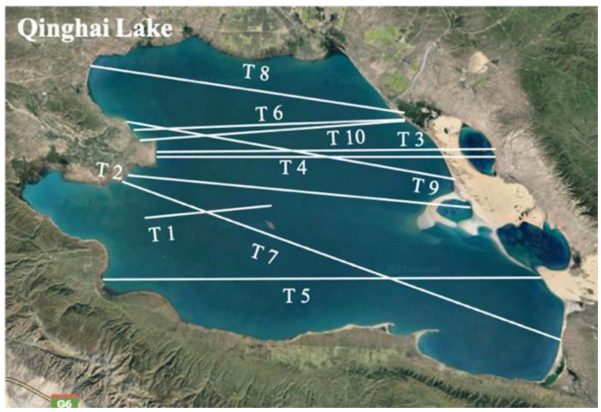

Fig. 1. Trajectories of specular reflection points of CYGNSS Qinghai Lake L0 data in 2018.

CYGNSS each raw dataset consists of raw IF data file and its metadata file: The raw IF data file consists of three sets of raw signal sample streams (duration approximately 1 min). The zenith antenna receives direct signals, and the port and starboard antennas receive reflected signals; meta data files provide auxiliary information, such as CYGNSS SC, instruments, and timing information. The bandwidth of CYGNSS raw signal is about 2.5 MHz, with 3.8724 MHz as the center frequency and 16.0362 MHz as the sampling frequency [27]. The track of mirror points collected by the raw data passes through Qinghai Lake (Table I). The trajectory of specular reflection points is shown in Fig. 1.

B. Raw IF Data Processing Method

At present, spaceborne GNSS-R L1 data are mainly used to realize GNSS-R inversion, and there are few studies on the raw IF data of spaceborne GNSS-R. Compared with GNSS-R L1 product data, using a software-defined receiver to process the raw IF data of GNSS-R can extract more potential information (such as interferometric carrier phase observations, residual Doppler observations, etc.), to mine more information about the physical characteristics of the reflector, to obtain higher resolution tracking related results, and the inversion results have higher accuracy and higher temporal and spatial resolution.

The processing of CYGNSS raw IF signal is shown in Fig. 2, which mainly includes three parts. The first part includes segmented acquisition of the reflected IF signal and acquisition, tracking and decoding of the direct signal using a software receiver. Since the cycle of the C/A code is 1 ms, the code phase of the reflected signal per millisecond can be obtained through correlation calculation. The second part is the extraction, correction, and compensation of the code phase, including geometric calculation based on the input orbit data. There is a certain difference in code phase extraction between the direct signal and the reflected signal. The direct type can stabilize the

TABLE I
RAW IF DATA RECORD OF QINGHAI LAKE IN 2018

Track	Raw IF data (UTC)	PRN	CYGNSS ID	Surface condition	Incidence angle
1	2018.02.01 S:16:33:13–E:16:33:44	17	SC 03	Ice	25.9°–26.0°
2	2018.02.20 S:08:56:44–E:08:57:44	16	SC 06	Ice	31.8°–31.6°
3	2018.03.08 S:00:43:41–E:00:44:41	10	SC 05	Ice	27.3°–27.6°
4	2018.03.19 S:19:02:30–E:19:03:30	05	SC 06	Ice	27.6°–27.3°
5	2018.03.30 S:13:42:57–E:13:43:57	17	SC 04	Mixed ice and water	27.7°–27.1°
6	2018.03.30 S:13:42:57–E:13:43:57	19	SC 04	Mixed ice and water	25.0°–25.1°
7	2018.04.20 S:05:27:12–E:05:28:12	09	SC 01	Water	68.2°–67.5°
8	2018.05.11 S:18:58:20–E:18:59:20	15	SC 05	Water	45.3°–45.1°
9	2018.05.14 S:17:26:20 -E17:27:20	13	SC 04	Water	45.4°–45.0°
10	2018.05.29 S:08:51:46–E:08:52:49	17	SC 07	Water	25.1°–25.2°

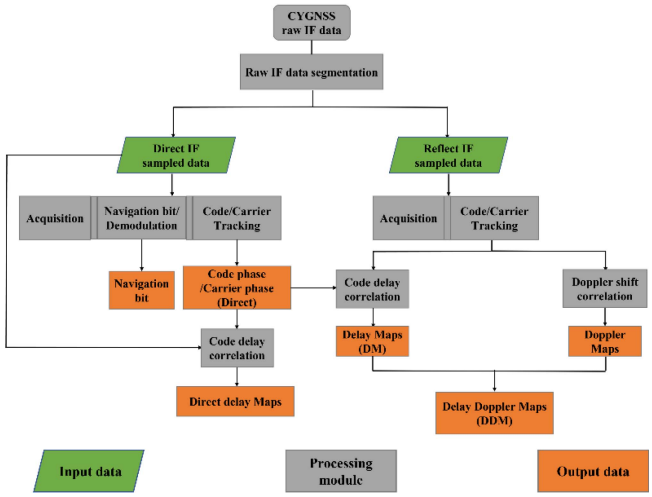

Fig. 2. CYGNSS raw IF data processing flow chart.

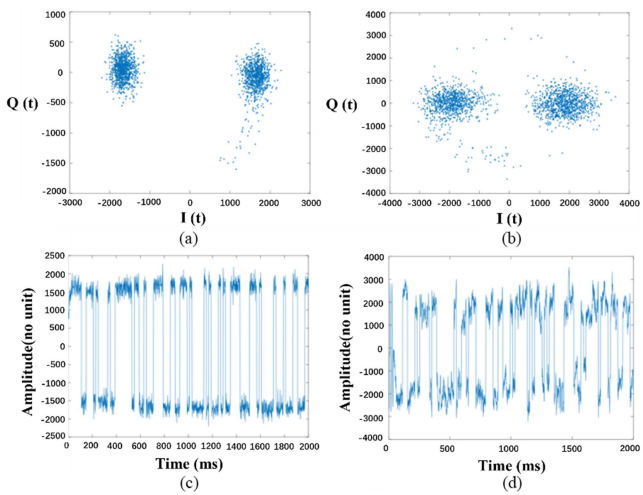

Fig. 3. CYGNSS raw IF data tracking results. (a) Direct signal Lissajous figure. (b) Reflected signal Lissajous figure. (c) Direct signal navigation bit. (d) Reflected signal navigation bit.

output code phase during the tracking phase, while the reflected signal needs to be accumulated coherently and noncoherently. The tracking results of the direct signal and reflected signal are shown in Fig. 3.

When the software receiver is in a stable tracking state for the signal, the carrier phase and code phase of the direct signal and reflected signal can be obtained. The main output of the processing is the complex waveform of the reflected signal, which can be either conventional GNSS-R DDM two-dimensional (2-D) power calculation processing or interference processing. However, in this article and the provided data products, only the conventional GNSS-R DDM 2-D power calculation process is presented. For each GNSS satellite, its complex waveform is computed by correlating the reflected signal with a set of locally generated clean copies

$$\mathrm{DDM}(t0,\Delta\tau i)=\int_0^{tc} s^r(t0+t1)c\left[\Phi^r_{\mathrm{code}}(t0+t1)+\Delta\tau i\right] \times e^{-2\pi j\left[f^r_{\mathrm{carr}}(t0)t1+\phi^r_{\mathrm{carr}}(t0)\right]}dt. \tag{1}$$

In the formula, t_0 is the intercorrelation start time of each complex waveform, $\Delta\tau_i$ is the time delay of each waveform lag, t_c is the coherent integration time, $c(\cdot)$ is the PRN code sequence generated by the local end after the navigation bit correction, s^r is the reflected signal, Φ^r_{code} is the code phase of the PRN code generated by the local end, f^r_{carr} and $\varphi^r_{\mathrm{carr}}$are the frequency and phase of the carrier copy generated by the local numerically controlled oscillator (NCO), respectively

$$\Delta\tau=\frac{f_{\mathrm{NCO}}\times 2^q}{f_s}+f_{\mathrm{Doppler}}-f_c \tag{2}$$

$$f^r_{\mathrm{carr}}=\frac{\mathrm{rate\_}c\times k}{fs}. \tag{3}$$

In formula (2), f_{NCO} is the local carrier replication frequency simulated by the NCO, q is the number of NCO register bits used in the software receiver tracking module, and the number of register bits of the software receiver designed in this article for 32. f_c is the center frequency, f_s is the corresponding sampling frequency, and f_{Doppler} is the set Doppler frequency shift. The highest resolution of the Doppler dimension of the correlation results generated by CYGNSS raw IF data is 1 Hz and there

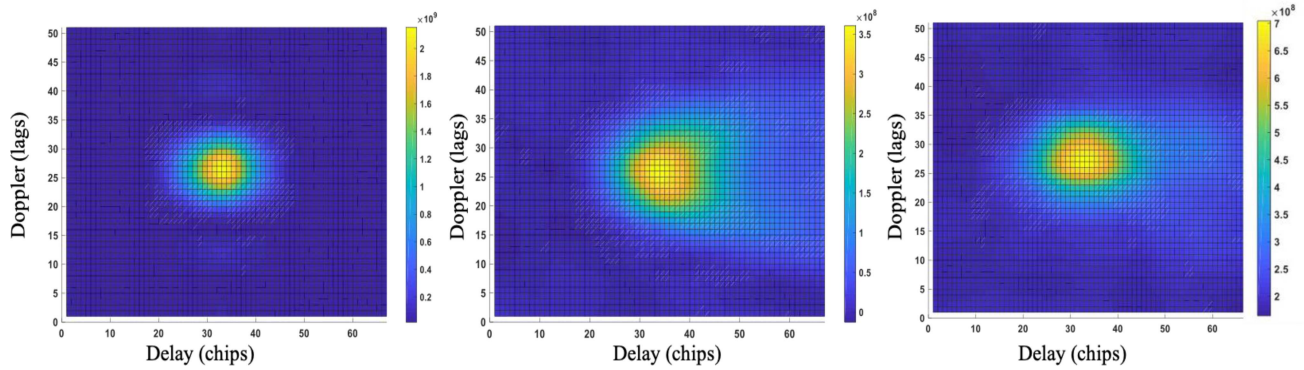

Fig. 4. 100 ms incoherent DDM (from left to right is lake ice, lake, and land).

is no minimum resolution limit. The resolution of the Doppler dimension of the DDM generated in this article is 100 Hz.

In formula (3), rate_c = 1.023 MHz represents the code frequency of GPS, and k is the correlation step size. The time delay resolution of the correlation result can be controlled by adjusting the value of k. For example, when $k = 4$, the time delay resolution of the correlation result is 0.25 chips (CYGNSS compressed DDM resolution). The sampling frequency of CYGNSS remote sensing satellite is about 16 MHz, that is, about 16 000 samples per millisecond, and each chip can obtain 16 samples, corresponding to the highest delay resolution of 1/16 chips, and the lowest delay resolution is 1/2 chips to satisfy the limit of the Nyquist sampling frequency.

When correlating the reflected signal, due to the roughness of the reflecting surface, the reflected signal is affected by noise to varying degrees. When correlation processing fails to obtain an obvious peak, it is necessary to perform coherent integration and noncoherent integration on the correlation results after tracking. The coherent and noncoherent integrals are defined as

$$I\text{Coh} = \sum_{i=1}^{n} I_i \quad Q\text{Coh} = \sum_{i=1}^{n} Q_i \tag{4}$$

$$P\text{Incoh} = \sum_{j=1}^{m} \left(\left(I_{\text{Coh}}^{j} \right)^2 + \left(Q_{\text{Coh}}^{j} \right)^2 \right). \tag{5}$$

Formula (4) is to calculate the coherent integral of 1 ms, where I_i and Q_i represent the sampling values of I branch and Q branch, respectively, and n is the number of sampling points per millisecond.

Formula (5) is based on the per millisecond coherent integration result calculated in (4) and calculates the noncoherent integration result for a certain period, which is 100 ms in this article. In the formula (5), the coherent value I_{coh} of the I branch and Q_{coh} of the Q branch can be noncoherently accumulated to obtain the related power P_{incoh}. The 2-D correlation power calculation result is shown in Fig. 4.

C. Validation of Raw IF Data

In 2018, the DDM incoherence time of CYGNSS L1 data was 1000 ms. To verify the correctness of the relevant results, the DDM generated from software receiver using CYGNSS raw IF data was compared with the CYGNSS compressed DDM. The data recorded by CYGNSS Qinghai Lake reflection event are between 16:33:13 and 16:33:44 (UTC) on February 1, 2018, the raw data stream received by CYGNSS 03 satellite, and the transmitted signal satellite is GPS PRN 17. Fig. 5 shows the position of the specular point.

Fig. 5. CYGNSS lake reflection event specular point.

Fig. 6(a) is the time-delay Doppler power spectrum generated from software receiver by using CYGNSS raw IF data corresponding to the abovementioned lake reflection event. The delay range is from −2 chips to 2 chips; the Doppler range is from −2500 to 2500 Hz. Fig. 6(b) shows the corresponding 0 Hz Doppler delay power spectrum (DM) slice results. Fig. 6(c) and (d) is CYGNSS compressed DDM data and 0 Hz DM slices.

This article uses the Pearson correlation coefficient to quantitatively verify the correctness of the correlation results. The definition of the Pearson correlation coefficient r is as follows:

$$r = \frac{\sum_{i=1}^{n} \left(X_i - \overline{X} \right) \left(Y_i - \overline{Y} \right)}{\sqrt{\sum_{i=1}^{n} \left(X_i - \overline{X} \right)^2} \sqrt{\sum_{i=1}^{n} \left(Y_i - \overline{Y} \right)^2}}. \tag{6}$$

In the formula, X_i and Y_i, respectively, represent the correlation result of CYGNSS raw IF data processed by the software receiver and the value of CYGNSS compressed DDM. $\bar{X}$ and $\bar{Y}$ are the mean value of the correlation results of CYGNSS raw IF data and the mean value of CYGNSS compressed DDM, respectively. After the Pearson correlation test, the correlation result

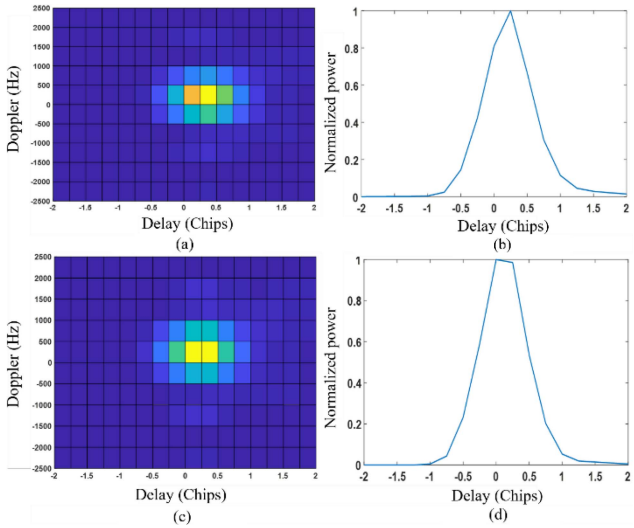

Fig. 6. Correlation results of raw IF data of CYGNSS ice surface reflection events compared with L1 results. (a) Raw IF data DDM. (b) Raw IF data DM. (c) L1 data DDM. (d) L1 data DM.

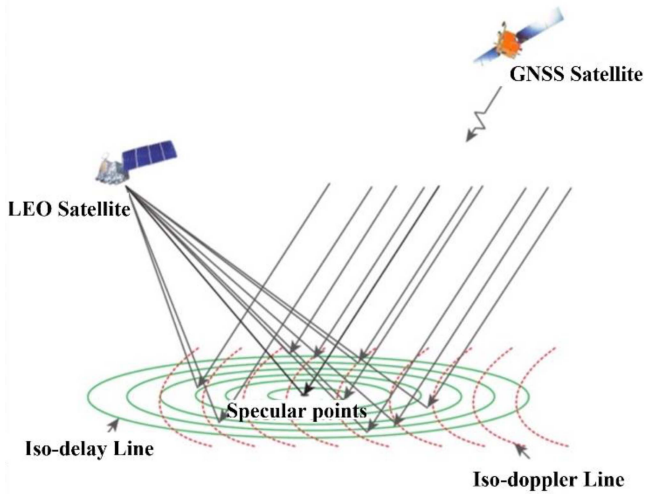

Fig. 7. Geometric model of spaceborne GNSS-R bibase radar.

of the raw IF data corresponding to the Qinghai Lake reflection event and the compressed DDM Pearson correlation is 0.935, which proves that the tracking results of the carrier tracking loop designed in this article are correlated, the correctness of the calculation satisfies the conditions for further inversion.

III. Principles of Spaceborne GNSS-R Lake Detection

A. Spaceborne GNSS-R Scattering Principle

Fig. 7 shows geometric model of spaceborne GNSS-R bistatic radar. In most GNSS-R observation scenarios, due to the diffuse reflection of the signal on the sea surface, the carrier phase of the GNSS reflection signal will be randomly superimposed at the receiver, and will change dynamically with the observation process, so the coherent integration of the GNSS reflection signal, and the time should not be too long. In addition, the random phase variation will cause the power of the received signal to fluctuate and generate speckle noise. Therefore, a short-time (usually 1 ms) coherent integration and a longer time (usually 1000 ms) incoherent accumulation of the reflected signal is usually performed to obtain the correlation power. A coherent signal is one in which the specular point reflects most of the signal with the same phase offset. Incoherent scattering occurs when GNSS signals are scattered from surfaces whose height changes greater than the L-band wavelength (∼19 cm); conversely, coherent reflection occurs when reflected from surfaces with height change smaller than the wavelength, so the coherent reflected signal is usually generated by the specular reflection of the GNSS signal. The coherent reflection zone is the first Fresnel zone around the specular point, and its range changes with the geometric position relationship between GNSS satellites, low-orbit GNSS-R satellites, and mirror points. Surface coverage types, terrain, and surface roughness will cause GNSS signals to appear incoherent scattering. The surface of ice and land is calmer and smoother than lake, making scattering characteristics of GNSS-R signals to be used to realize the detection of lake boundaries [18]. This article mainly uses PR and D_{LR} for coherence analysis.

B. Coherence Detection Based on PR Threshold

The raw count DDM (uncalibrated) undergoes two-stage calibration of thermal noise, antenna gain, and antenna pattern to generate a bistatic radar cross-section. The power of coherent reflection and incoherent scattering are both observable. However, the actual measurement data have complex components, including coherent, incoherent, and coherent and incoherent mixtures. DDM with noise ratio is classified as incoherent signal, and DDM with coherent or coherent reflection dominance is classified as coherent signal. At present, most of the research on lake detection are based on the signal-to-noise ratio of the direct signal and the reflected signal, the slope of the leading edge, the slope of the trailing edge, etc. In this article, based on the power spread detection (DDM power-spread detector) method proposed in [20], the power distribution is estimated by PR, and the calculation is as follows:

$$\mathrm{PR} = \frac{C_{\mathrm{in}}}{C_{\mathrm{out}}} \tag{7}$$

$$C_{\mathrm{in}} = \sum_{i=k1}^{k2} \sum_{j=l1}^{l2} \mathrm{DDM}\left(\tau_M + i, f_M + j\right) \tag{8}$$

$$C_{\mathrm{out}} = \sum_{i=1}^{N_\tau} \sum_{j=1}^{N_f} \mathrm{DDM}\left(i, j\right) - C_{\mathrm{in}} \tag{9}$$

where C_{in} is the total power of the delay-Doppler region around the mirror point of the raw counting DDM; C_{out} is the total power of all DDM pixel units except C_{in}; $N\tau$ and N_f are the delay-dimensional and Doppler-dimensional units, respectively; and τ_M and f_M represent the time delay corresponding to the maximum value of DDM and the position of the Doppler pixel, respectively. For coherent reflection, the received reflection power is mainly concentrated in C_{in}, while the power in C_{out} is small, so PR is relatively large. The DDM generated by

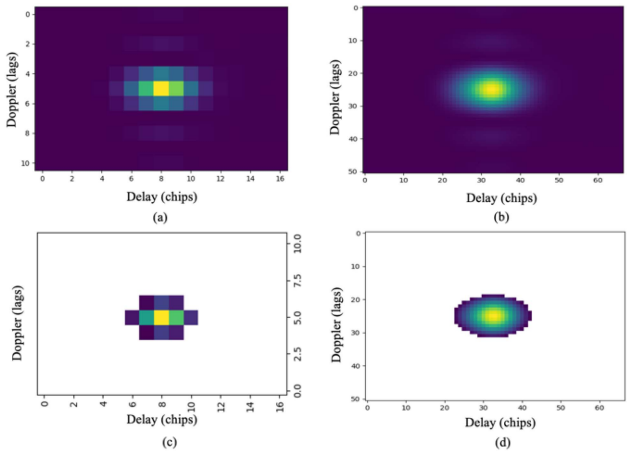

Fig. 8. Comparison between the CYGNSS Level-1 DDM and Raw IF data before and after thermal noise removal.(a) CYGNSS Level-1 DDM before removing thermal noise. (b) CYGNSS raw IF data DDM before removing thermal noise. (c) CYGNSS LEVE-1 DDM after removing thermal noise. (d) CYGNSS raw IF data DDM before removing thermal noise.

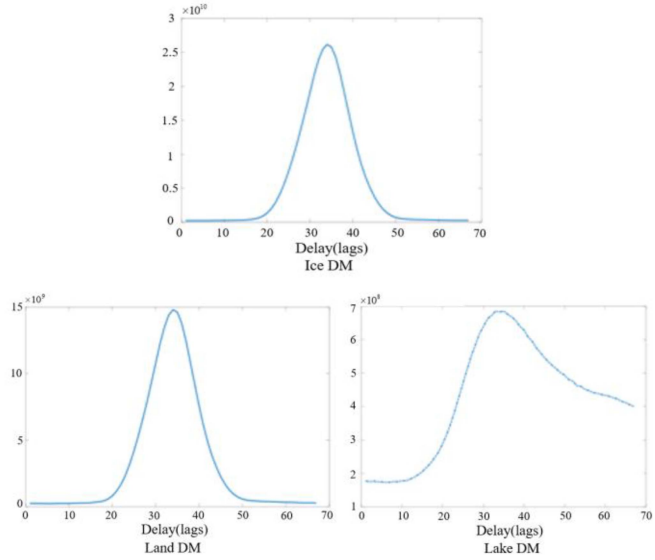

Fig. 9. High-resolution DM comparison of ice, land, and lake.

incoherent scattering mostly presents a typical horseshoe shape, and the power spreads to other pixel units, resulting in a decrease in PR. In addition, some pixel units of the raw count DDM cannot be mapped to the Earth's surface, and these unmappable DDM pixel units mainly contain thermal noise. Since these pixel units convey inconsistent information, they are removed from C_{out}. The thermal noise exclusion empirical function proposed in [20] is used for removal.

Among them, for CYGNSS L1 DDM (17 × 11 dimension) parameters $k1$, $k2$, $l1$, and $l2$ in (8) are -1, 1, -2, and 2, respectively, that is, C_{in} is 3 × 5 delay Doppler around the mirror point of raw counting DDM. The high-resolution raw count DDM generated by processing the raw IF data with a software receiver is composed of 67 delays (delay resolution: 0.0625 chips) × 51 Doppler frequency (Doppler resolution: 100 Hz), improving the delay dimension by 4 times and the Doppler dimension by 5 times. Under this condition, the selected C_{in} range is 12 × 25 around the specular reflection point of the high-resolution DDM, including the main power of the received DDM. Fig. 8 shows CYGNSS compressed DDM and CYGNSS raw IF data high-resolution DDM before and after thermal noise removal contrast, the same specular point (36°83'N, 99°57'E), and the state of the specular reflection point is an ice surface. The PR value of CYGNSS compressed DDM is 3.2943, and the PR value of CYGNSS raw IF data high-resolution DDM is 0.6628.

Literature [20] obtained the statistical results of CYGNSS L1 DDM through a large amount of data statistics. The optimal classification threshold of coherent and noncoherent DDM is 2, that is, when PR $\geq$ 2, DDM presents coherent reflection; when PR $<$ 2, DDM exhibits incoherent scattering. For the high-resolution DDM generated by CYGNSS raw IF data, the lower threshold is 0.5, that is, when PR $\geq$ 0.5, DDM presents coherent reflection; when PR $<$ 0.5, DDM presents incoherent scattering. Due to the high roughness of the lake, its incoherent scattering accounts for a larger proportion, and the PR value is usually less than 0.5 (the average value of the lake is about 0.35, and the average value of the land is about 0.42). On the contrary, the coherent reflection of the lake ice is more obvious, and the PR values are generally greater than 0.5. Therefore, this article combines many PR results and uses 0.5 as the PR threshold to effectively detect lake ice.

C. Detection of Effective Delay Distance

In spaceborne GNSS-R remote sensing, to identify the lake boundary more simply and accurately, this article first studies the characteristics of DDM in the delay domain (delay map, DM) to identify lake ice, lake, and land expressed as

$$|Y_{\text{DM}}(\tau)|^2 = |Y_{\text{DM}}(\tau, f_0)|^2. \tag{10}$$

In the formula (10), f_0 is the Doppler frequency when $|Y_{\text{DM}}(\tau, f_0)|^2$ takes the peak value.

Affected by factors, such as antenna, instrument system noise, and signal transmission environment changes, DM data contain a large amount of irrelevant noise. To eliminate noise, the DM data between the left and right thresholds are taken as effective data, which are defined as the effective area S [21].

To obtain the effective area S, it is necessary to set the corresponding threshold to remove the noise from the DM data. However, due to the strong randomness of factors, such as antenna, instrument system noise, and signal transmission environment changes, and according to the above analysis, the correlation power between lake ice–lake and lake ice–land is quite different. Elimination of noise is prone to the problem that the effective area S is too large or too small. Therefore, this article uses an adaptive threshold adjustment algorithm to adjust the threshold value all the time.

High-resolution DM comparison of lake ice, land, and lake surface is shown in Fig. 9. The method of the adaptive threshold adjustment algorithm is taking the DM average value as a reference, expanding from the specular reflection point (that is, the delay coordinate corresponding to the DM peak power) to

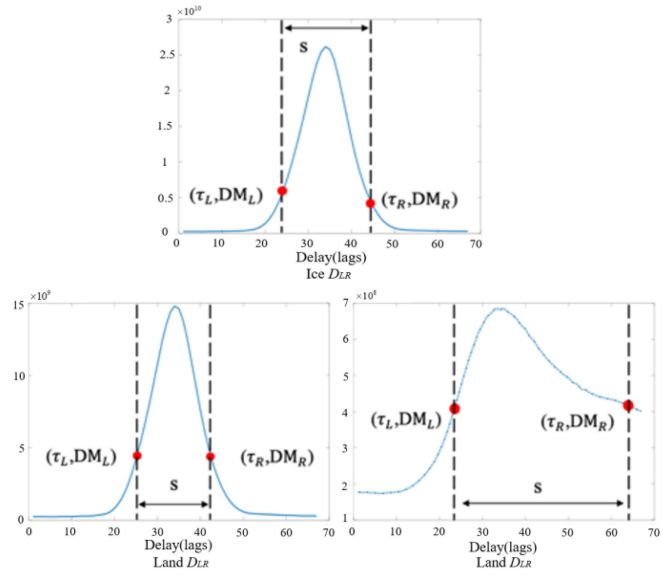

Fig. 10. Map of high-resolution DM effective area of lake ice, land, and lake.

both sides, and looking for the point lower than the average value for the first time, denoted as (τ_L, DM_L) and (τ_R, DM_R); the DM data between the two points are taken as the effective correlation power value. To verify its effectiveness, a group of DMs containing lake ice, lake, and land were randomly selected from the processing results for comparison. It can be seen from Fig. 10 that the algorithm can automatically adjust the threshold value according to different DM data to obtain effective correlation power values.

The effective delay distance D_{LR} is defined as

$$D_{\mathrm{LR}} = \tau_R - \tau_L. \tag{11}$$

According to the above calculation method, in the three reflection event cases in Fig. 10, the effective zone delay distance D_{LR} of lake ice, land, and lake is 1.625, 1.5625, and 2.4375 chips, respectively. Due to the smooth lake ice and land reflection surface, the delay wave after DM is relatively smooth, and the delay distance in the effective area is in the range of 1.5–1.7 chips. However, due to the rough reflective surface of the lake, there is an obvious "upturned" phenomenon in the postlayout, and D_{LR} of the effective area of the lake is significantly greater than the delay distance of the effective area between the ice and the land. This article uses high-resolution DDM data statistics, using $D_{\mathrm{LR}} = 2$ chips as the threshold to further detect lake surface.

D. Inversion Flow Chart

Fig. 11 is the inversion flow chart of this article. In the data preprocessing step, the data of the specular reflection point located in Qinghai Lake are screened out through auxiliary information, such as the time of CYGNSS L1 data, longitude, and latitude, and then the corresponding CYGNSS is screened out through matching raw IF data. In the step of building the model, calculate and establish the PR and D_{LR} according to

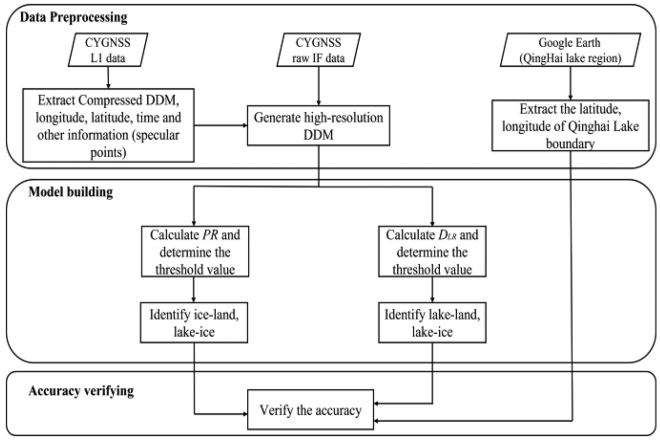

Fig. 11. Inversion flow chart.

the methods in Sections II- B and C, and finally verify the accuracy of result by calculating the minimum distance between the identified specular points and the boundary points extracted by Google Earth.

The spatial resolution of GNSS-R mainly includes the spatial resolution of mirror point distribution and sampling spatial resolution. Between them, the spatial resolution of specular point distribution is mainly determined by the number of reflected signals received by GNSS-R satellite. The spatial resolution of sampling mainly depends on the spatial resolution of the spectrum (pulse limited footprints) and the sampling time along the track. The sampling spatial resolution determines the minimum area of the grid when calculating the spatial resolution of mirror point distribution [31]. Since this article mainly realizes lake boundary detection in Qinghai Lake region, the spatial resolution of specular point distribution is adopted as the reference standard in this article.

By using software receiver, the spatial resolution of CYGNSS DDM could be further improved through integration time. By using 100 ms, the spatial resolution of land surface can be improved from 7 km × 5 km to 0.7 km × 0.5 km. It can further improve the accuracy of lake boundary detection, which is conducive to the development of terrestrial GNSS-R application.

IV. Results and Analysis

A. Analysis of PR Values at Different Incoherent Integration Times

A group of ice reflection events Case 1 (No 2 in Table I) and a group of lake reflection events Case 2 (No 7 in Table I) were selected to further analyze the influence of integration time on the PR value. Among them, the raw IF data stream corresponding to the reflection event of Case 1 was recorded at 08:56:44–08:57:44 on February 20, 2018, and the raw IF data stream corresponding to the reflection event of case 02 was recorded at 08:51:46–08:52:49 on May 08, 2018. The specular reflection points corresponding to Case 1 and Case 2 are shown in Fig. 12.

Under the same high-resolution DDM dimension (67 × 51), the integration time was set to be 100, 500, and 1000 ms,

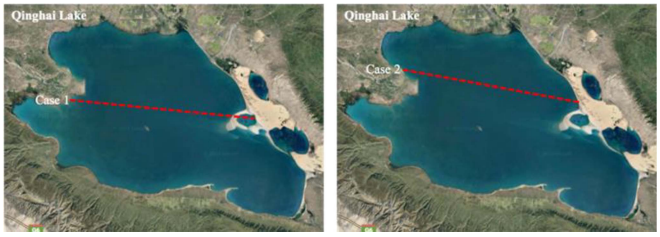

Fig. 12. Case 1 and Case 2 specular reflection point trajectories, ice(left), lake(right).

respectively, and the corresponding PR values were calculated for the mirrors under the trajectory of the two groups of specular reflection points, respectively. The calculated PR values are shown in Fig. 13.

It can be seen from Fig. 13 that under different integration time conditions, when the specular reflection point is the lake ice, the PR value fluctuates between 0.6 and 0.75; when the specular reflection point is the lake, the PR value fluctuates between 0.25 and 0.4; when the specular reflection point is the lake, the PR value fluctuates between 0.3 and 0.5; it can be concluded that the integration time has little effect on the PR value calculated by DDM.

From the left figure of Fig. 13 (Case 1), under different integration times, PR can effectively distinguish lake and lake ice. Even in the DDM map of 100 ms, proving that the PR $=$ 0.5 threshold is valid. However, due to the more similar PR characteristics between the lake and the land, it can be seen from the right figure (Case 2) that in the 1000 and 500 ms DDM pictures, the PR change of the lake and the land boundary area is more obvious, but in the 100 ms DDM picture, the change of PR in the boundary area with the land is relatively vague, indicating that in the case of 100 ms integration time, the PR $= 0.5$ threshold cannot distinguish the lake and land very well, especially in the boundary area between the lake and the land.

It can be seen in Fig. 13 that 100 ms has more dense effective data, and results with higher spatial resolution can be calculated.

B. Analysis of DLR Values at Different Incoherent Integration Times

To further detect the boundary between the lake and the land, this article further uses D_{LR} as an important method for lake detection, and the impact of different incoherent times on D_{LR} is also explored. The inversion case is the same as the inversion case in Section II. The results of D_{LR} under different noncoherent integration times (100, 500, and 1000 ms) are as follows.

It can be seen from Fig. 14 that under different integration time conditions, when the specular reflection point is ice (Case 1), the D_{LR} of the lake ice is very close to D_{LR} of the land, both of which are 1.4–1.7; when the specular point is the lake (Case 2), the D_{LR} value is above 2; it can be concluded that the integration time has little effect on D_{LR} calculated by DDM.

From the right figure (Case 2) in Fig. 14, D_{LR} of the lake and the land is quite different. Generally, under different integration times, D_{LR} can effectively distinguish the lake from the land, which proves that the $D_{\mathrm{LR}} = 2$ threshold is effective. However, the lake ice and the land have more similar D_{LR} characteristics, the $D_{\mathrm{LR}} = 2$ threshold cannot distinguish lake ice and the land very well when the integration time is 100 ms, especially in the boundary area between lake ice and land.

Also, in Fig. 14, 100 ms has more dense effective data, and results with higher spatial resolution can be calculated.

C. Feasibility Analysis of Lake and Lake Ice Detection

In Case 3 (Track 6 of Table I), the raw IF data stream corresponding to the reflection event in Case 3 was recorded at 13:42:57–13:43:57 on March 30, 2018, and Qinghai Lake is in a state of melting ice. The trajectory of its specular reflection points is shown in Fig. 15. The raw IF data were combined into 92 high-resolution DDMS by noncoherent accumulation of 100 ms, corresponding to 92 specular points of 0.7 km spatial resolution.

The PR value of Case 3 is shown in Fig. 16. The results of the inversion method are consistent with the actual situation of Qinghai Lake melting ice, showing a state of ice and water mixing [32]. The reflection area of the ice surface can be distinguished through Fig. 16 combined with the threshold analysis of PR value. However, there is no ground truth to prove the validity of the results. It is proved that GNSS-R raw IF data could further distinguish between ice surface and water surface.

D. Boundary Detection Result

According to the analysis results of Section III, using the raw IF data collected near Qinghai Lake in 2018 published by the CYGNSS website (https://podaac.jpl.nasa.gov/CYGNSS) and the surface water dataset of global land analysis and discovery (GLAD) generated by Landsat 5, 7, and 8 scenes (https://glad.umd.edu/dataset/global-surface-water-dynamics) for lake boundary detection and analysis. First, the software receiver was used to generate the available 100 Hz DDM (51×67) from the raw IF data of CYGNSS, and the combination of PR and D_{LR} was used to realize the boundary detection of Qinghai Lake.

Two extraction methods of lake boundary are used to compare and verify the detection accuracy of this article. Data sources are from Google Earth and the surface water dataset of GLAD in 2018 [33], respectively.

Figs. 17 and 18 show the boundary extraction results of Qinghai Lake in 2018. At the same time, the latitude and longitude of the shoreline of the Qinghai Lake area were extracted from Google Earth and surface water dataset of GLAD.

To analyze the CYGNSS lake boundary and the error between inversion results and real boundary more accurately, Tables II and III, respectively, counted the reflecting surface, data volume, and mean PR and D_{LR} results of specular points derived from raw IF data of CYGNSS.

Since the energy value of the GNSS reflection signal reflected by the ice surface is much larger than that of the land and the lake (as shown in Fig. 4), the PR threshold of 0.5 can effectively distinguish the lake ice–lake and lake ice–land, but it is difficult to distinguish the lake and land. Considering that the D_{LR} of

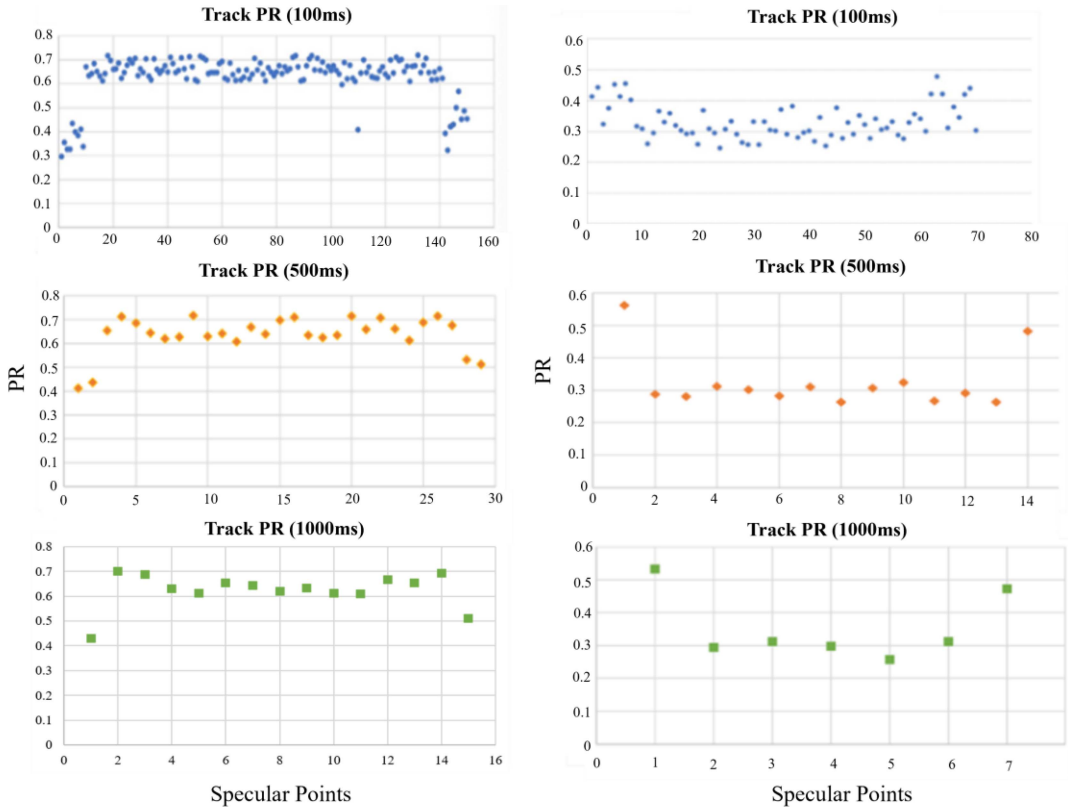

Fig. 13. PR values under different integration times in Case 1 (left) and Case 2 (right).

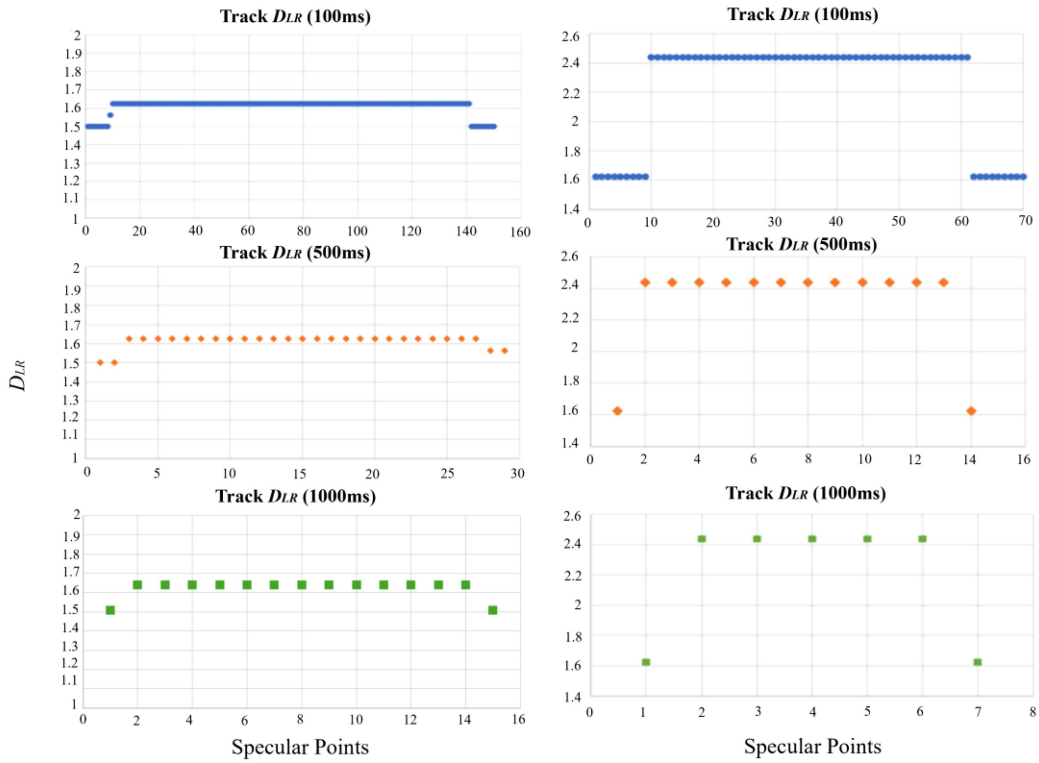

Fig. 14. D_{LR} values under different integration times in Case 1 (left) and Case 2 (right).

Fig. 15. Ice–water mixed reflection event specular reflection point trajectory.

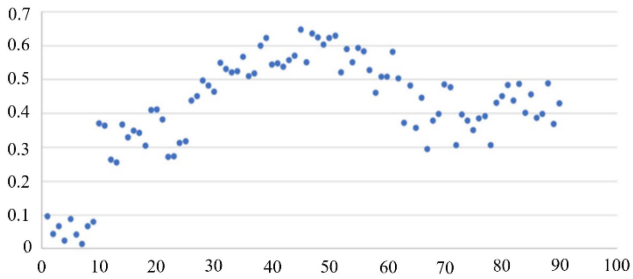

Fig. 16. PR value of mixed reflective surface of ice and water.

Fig. 17. Google Earth boundary extraction results of Qinghai Lake.

TABLE II
INVERSION RESULTS OF PR VALUE (THRESHOLD = 0.5)

Datasets	Surface	Data volume/group	*PR* mean
Raw IF data	Lake	438	0.376
	Lake ice	476	0.673
	Land	42	0.411

the lake is significantly larger than that of the land and lake ice due to its rough reflective surface (as shown in Fig. 7), the D_{LR} threshold of 2 can effectively distinguish the lake–land and lake–lake ice. Thus, combining the two methods can realize the identification of the three reflective surfaces.

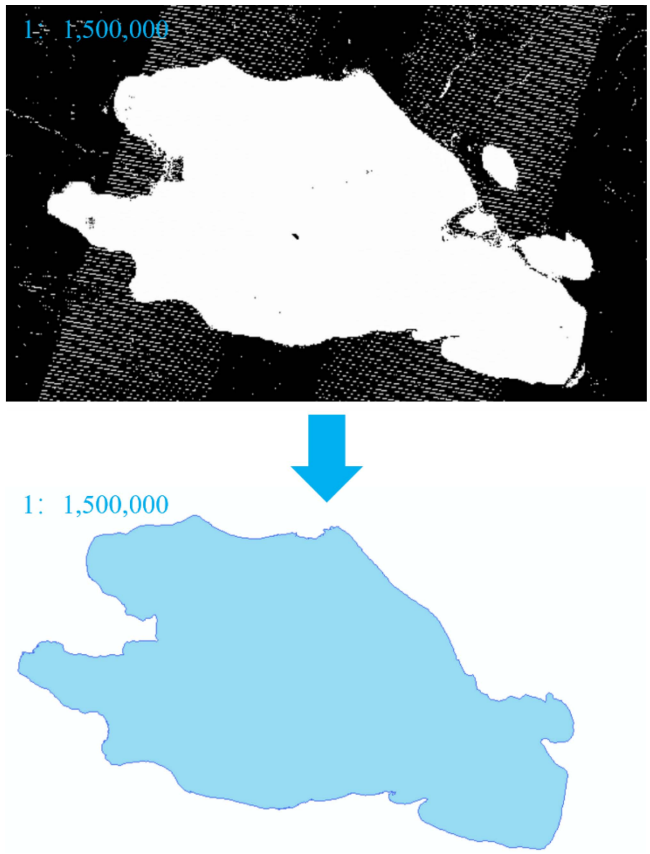

Fig. 18. GLAD boundary extraction results.

TABLE III
INVERSION RESULTS OF DLR (THRESHOLD = 2)

Datasets	Surface	Data volume/group	D_{LR} mean
Raw IF data	Lake	438	2.433
	Lake ice	476	1.524
	Land	42	1.552

In this article, the minimum distance detected is used as the accuracy verification standard, and the calculation formula of the distance D between the latitude and longitude of two points is as follows:

$$\mathrm{D} = 111.12 \cos\{1/[\sin(\Phi_A)\sin(\Phi_B) + \cos(\Phi_A)\cos(\Phi_B)\cos(\lambda_B - \lambda_A)]\} \quad (12)$$

where A is the specular reflection point considered as the boundary, and the corresponding longitude and latitude are λ_A and Φ_A, respectively. B is the referenced boundary point extracted from Google Earth, and the corresponding longitude and latitude are λ_B and Φ_B, respectively. The minimum value $D_{\min}$ is taken as the error. The corresponding results are shown in Table IV. Since the original IF data damage of Track1 can only Track 3.5s, the inversion results of Track 1 are removed.

According to the inversion results in Figs. 17 and 18, and Tables II, III, and IV, the combined use of PR and D_{LR} can

TABLE IV
BOUNDARY POSITION CALCULATION ERRORS

Track ID	Left boundary error /km (Google Earth)	Right boundary error /km (Google Earth)	Left boundary error /km (GLAD)	Right boundary error /km (GLAD)
Track 2	0.421	0.533	0.446	0.571
Track 3	0.322	0.682	0.301	0.657
Track 4	0.478	0.424	0.455	0.439
Track 5	0.513	0.561	0.484	0.607
Track 6	0.534	0.651	0.517	0.676
Track 7	0.547	0.337	0.579	0.416
Track 8	0.652	0.672	0.634	0.697
Track 9	0.673	0.389	0.663	0.419
Track 10	0.371	0.632	0.442	0.684

realize the detection of lake boundaries. Experimental results show that the space-borne GNSS-R PR method adopted in this article can effectively detect the boundary of lake ice–lake and lake ice–land, and the spaceborne GNSS-R D_{LR} method can effectively detect the boundary of lake–lake ice and lake–land. Measurements using Google Earth and GLAD data were consistent. The inversion errors are all smaller than 0.7 km (the spatial resolution distance of high spatiotemporal resolution DDM), which satisfies the inversion accuracy. It can be seen from the results in Table IV that the raw IF data of CYGNSS is in good consistency with the boundary detection results of Google Earth and GLAD product data. Except for the specular points of Track1, the detection results of specular points of all other trajectories are less than 700 m, which meets the conditions for edge detection.

V. CONCLUSION

This article proposes a lake boundary detection method based on spaceborne GNSS-R and gives the processing method of CYGNSS raw IF data and the general process of DDM data processing under spaceborne experimental conditions. Specular points combined with Google Earth and GLAD product data are used to conduct a verification test; the results show the following conditions.

1) Compared with CYGNSS L1 data, using CYGNSS raw IF data and setting different integration times can effectively improve the spatial resolution of spaceborne GNSS-R reflection signals. The detection distance is increased from 7 to 0.7 km, which can theoretically achieve higher detection accuracy in space detection.
2) Both spaceborne GNSS-R PR and DM effective area delay distance D_{LR} can effectively detect lake boundaries: the PR method can effectively distinguish lake ice–lake and lake ice–land boundaries, and the D_{LR} method can effectively distinguish lake–lake ice and lake–land boundaries. The lake boundary detection errors are all within 0.7 km, meeting the needs of inversion.
3) This article uses CYGNSS raw IF data of the Qinghai Lake area in 2018 to carry out lake boundary detection for the first time. It proves that the raw CYGNSS IF data combined with PR and D_{LR} can be used for lake boundary detection. Spaceborne GNSS-R technology has the advantages of simple networking, high time resolution, low cost, and no weather influence. And it has great development potential in the field of lake boundary detection.

This article proves the feasibility of boundary detection by using CYGNSS raw IF data, but due to the scarcity of CYGNSS raw IF data and few specular reflection points, the complete boundary of Qinghai Lake cannot be obtained.

The change of river boundary is a very important characteristic quantity. The article [34] studied the Qinghai Lake water boundary dataset in the 11th period from 1987 to 2017, and the maximum change of the boundary point is less than 500 m. The original IF data of CYGNSS used in this article has a resolution of 700 m, and the variation range is smaller than the spatial resolution of the original IF data. It may be difficult to detect the rate of change of the boundary of Qinghai Lake using our method, and the rate of change may require longer time and more data to evaluate the change.

ACKNOWLEDGMENT

The authors would like to thank the NASA for providing the CYGNSS raw IF dataset, the Danish Technical University for providing the DTU18 global MSSH model, and the DTU global tide model. Thanks to Yang Dongkai and Wang Feng of Beijing University of Aeronautics and Astronautics and Li Weiqiang of CSIC-IEEC for their suggestions on GNSS-R satellite data analysis. We would like to thank engineer Zhou Bo and Sheng Zhichao of Shanghai Aerospace Electronics Institute for their suggestions on reflection signal receivers and river flow velocity inversion models and their assistance with the experiment.

REFERENCES

[1] T. M. Pavelsky and L. C. Smith, "RivWidth: A software tool for the calculation of river widths from remotely sensed imagery," *IEEE Geosci. Remote Sens. Lett.*, vol. 5, no. 1, pp. 70–73, Jan. 2008.
[2] L. Chengfeng, X. Changjun, and C. Yinxuan, "Remote sensing monitoring of water surface area change in Qinghai lake from 1974 to 2016," *J. Lake Sci.*, vol. 29, no. 5, pp. 1245–1253, 2017.
[3] J. Kittler, "On the accuracy of the sobel edge detector," *Image Vis. Comput.*, vol. 1, no. 1, pp. 37–42, 1983.
[4] D. Marr and E. Hildreth, "Theory of edge detection," *Proc. Roy. Soc. London B: Biol. Sci.*, vol. 207, no. 1167, pp. 187–217, 1980.
[5] X. Ren, "Multi-scale improves boundary detection in natural images," in *Proc. Eur. Conf. Comput. Vis.*, 2008, pp. 533–545.
[6] P. Dollar and C. L. Zitnick, "Fast edge detection using structured forests," *IEEE Trans. Pattern Anal. Mach. Intell.*, vol. 37, no. 8, pp. 1558–1570, Aug. 2015.
[7] W. Feng, Y. Pengyu, and Y. Dongkai, *GNSS-I/MR River boundary and Water Level Measurement: Theory and Simulation*. Beijing, China: Beijing Univ. Aeronaut. Astronaut., 2024, pp. 1–15.
[8] J. E. Coats et al., "Use of radars to monitor stream discharge by noncontact methods," *Water Resour. Res.*, vol. 42, no. 7, 2006, Art. no. W07422.
[9] D. R. Lyzenga, "Passive remote sensing techniques for mapping water depth and bottom features," *Appl. Opt.*, vol. 17, no. 3, pp. 379–383, 1978.

[10] H. Villadsen et al., "CryoSat-2 altimetry for river level monitoring-evaluation in the Ganges-Brahmaputra river basin," *Remote Sens. Environ.*, vol. 168, pp. 80–89, 2015.

[11] G. R. Brakenridge et al., "Space-based measurement of river runoff," *EOS Trans. Amer. Geophys. Union*, vol. 86, no. 19, pp. 185–188, 2013.

[12] W. Feng, Y. Pengyu, and Y. Dongkai, *GNSS-I/MR River boundary and Water Level Measurement: Theory and Simulation*. Beijing, China: Beijing Univ. Aeronaut. Astronaut., 2024, pp. 1–15.

[13] Y. Dongkai and Z. Qishan, *GNSS Reflected Signal Processing: Fundamentals and Applications*. Beijing, China: Publishing House of Electronics Industry, 2012.

[14] L. Weiqiang, E. Cardellach, F. Fabra, S. Ribó, and A. Rius, "Assessment of spaceborne GNSS-R ocean altimetry performance using CYGNSS mission raw data," *IEEE Trans. Geosci. Remote Sens.*, vol. 58, no. 1, pp. 238–250, Jan. 2019.

[15] Z. Yun et al., "Machine learning methods for spaceborne GNSS-R sea surface height measurement from TDS-1," *IEEE J. Sel. Topics Appl. Earth Observ. Remote Sens.*, vol. 15, pp. 1079–1088, Jan. 2021.

[16] Z. Yun et al., "High wind speed inversion model of CYGNSS sea surface data based on machine learning," *Remote Sens.*, vol. 13, no. 16, 2021, Art. no. 3324.

[17] W. Yanguang, B. Zhaoguang, Z. Xueping, W. Chongyu, and H. Lin, "Spaceborne GNSS-R sea surface wind field observation load key technology design and validation," *China's Space Sci. Technol.*, vol. 2, pp. 117–124, 2022, doi: 10.16708/j.cnki.1000-758X.2022.0029.

[18] Y. Songhua, G. Jianya, Z. Hun-shi, and L. I. Dong-xiu, "Ground-based experiment of GNSS-R measurement of surface soil moisture," *Chin. J. Geophys.*, vol. 54, no. 11, pp. 2735–2744, 2011.

[19] J. Ziying, Z. Bo, W. Jun, Y. Dongkai, and H. Xuebao, "Shore-based GNSS-R marine oil spill detection method," *J. Beijing Univ. Aeronaut. Astronaut.*, vol. 44, no. 02, pp. 383–390, 2018.

[20] Z. Guodong, G. Jian, Y. Dongkai, W. Feng, and G. A. O. Hongxing, "Spaceborne GNSS-R sea ice boundary detection method," *J. Wuhan Univ.*, vol. 44, no. 5, pp. 668–674, 2019.

[21] G. R. Brakenridge et al., "Space-based measurement of river runoff," *EOS Trans. Amer. Geophys. Union*, vol. 86, no. 19, pp. 185–188, 2013.

[22] C. D. Hall and R. A. Cordey, "Multistatic scatterometry," in *Proc. Geosci. Remote Sens. Symp.*, 1988, pp. 561–562.

[23] W. Li et al., "Lake level and surface topography measured with spaceborne GNSS-reflectometry from CYGNSS mission: Example for the lake Qinghai," *Geophys. Res. Lett.*, vol. 45, no. 24, pp. 13332–13341, 2018.

[24] E. Cardellach et al., "First precise spaceborne sea surface altimetry with GNSS reflected signals," *IEEE J. Sel. Topics Appl. Earth Observ. Remote Sens.*, vol. 13, pp. 102–112, Feb. 2019.

[25] T. S. Dahl-Jensen, O. B. Anderser, S. D. P. Williams, V. Helm, and S. A. Khan, "GNSS-IR measurements of inter annual sea level variations in Thule, Greenland from 2008–2019," *Remote Sens.*, vol. 13, no. 24, 2021, Art. no. 5077.

[26] W. Bai et al., "A first comprehensive evaluation of China's GNSS-R airborne campaign: Part II-river remote sensing," *Sci. Bull.*, vol. 60, no. 17, pp. 1527–1534, 2015.

[27] F. Wang, B. Zhang, D. Yang, W. Li, and Y. Zhu, "Sea-state observation using reflected Bei Dou GEO signals in frequency domain," *IEEE Geosci. Remote Sens. Lett.*, vol. 13, no. 11, pp. 1656–1660, Nov. 2016.

[28] Y. Zhang et al., "Research on shore-based river flow velocity inversion model using GNSS-R raw data," *Remote Sens.*, vol. 14, no. 5, 2022, Art. no. 1170.

[29] Y. Wang and Y. J. Morton, "Coherent reflections using closed-loop PLL processing of CYGNSS IF data," in *Proc. IEEE Int. Geosci. Remote Sens. Symp.*, 2019, pp. 8737–8740.

[30] M. Song et al., "Study on the exploration of spaceborne GNSS-R raw data focusing on altimetry," *IEEE J. Sel. Topics Appl. Earth Observ. Remote Sens.*, vol. 13, pp. 6142–6154, Oct. 2020.

[31] H. Dong and Y. Song, "Shrinkage history of lake Qinghai and causes during the last 52 years," in *Proc. Int. Symp. Water Resour. Environ. Protection*, 2011, pp. 446–449.

[32] M. Qi et al., "Monitoring the ice phenology of Qinghai lake from 1980 to 2018 using multisource remote sensing data and Google Earth Engine," *Remote Sens.*, vol. 12, no. 14, 2020, Art. no. 2217.

[33] A. H. Pickens et al., "Mapping and sampling to characterize global inland water dynamics from 1999 to 2018 with full Landsat time-series," *Remote Sens. Environ.*, vol. 243, 2020, Art. no. 111792.

[34] M. Y. Hao and Z. Luo, "Data set of Qinghai lake water boundary from 1987 to 2017," *Sci. Data China*, vol. 21, no. 01, pp. 191–197, 2012.

Yun Zhang received the Ph.D. degree in applied marine environmental studies from the Tokyo University of Maritime Science and Technology, Tokyo, Japan, in 2008.

Since 2011, he has been a Professor with the College of Information and Technology, Shanghai Ocean University, Shanghai, China. His research interests include the study of navigation system reflection signal technique and its maritime application.

Ziyu Yan received the M.S. degree in electronic information from the Shanghai Ocean University, Shanghai, China, in 2023. He is currently working toward the Ph.D. degree in electronic information with the Zhejiang University, Hangzhou, China.

His research interests include underwater acoustic signal processing and GNSS-R.

Shuhu Yang received the Ph.D. degree in physics from the School of Physics, Nanjing University, Nanjing, China, in 2012.

He is currently an Associate Professor with the College of Information Technology, Shanghai Ocean University, Shanghai, China. His research interests include maritime application using hyperspectral remote sensing, GNSS-R, SAR, and deep learning.

Wanting Meng received the B.S. degree in spatial information and digital technology and the M.S. degree in software engineering from the Shang Ocean University, Shanghai, China, in 2013 and 2016, respectively.

She is currently with the Shanghai Spaceflight Institute of TT&C and Telecommunication, Shanghai, China, where she is currently a Research Associate in the field of microwave radiometer calibration techniques and GNSS-R remote sensing.

Yanling Han received the B.E. degree in mechanical design and manufacturing and the M.E. degree in mechanical automation from the Sichuan University, Sichuan, China, in 1996 and 1999, respectively, and the Ph.D. degree in engineering and control theory from the Shanghai University, Shanghai, China, in 2005.

She is currently a Professor and is currently working with the Shanghai Ocean University, Shanghai, China. Her research interests include the study of ocean remote sensing, flexible system modeling, and deep learning.

Zhonghua Hong received the Ph.D. degree in GIS from the Tongji University, Shanghai, China, in 2014.

Since 2019, he has been an Associate Professor with the College of Information Technology, Shanghai Ocean University, Shanghai, China. His research interests include three-dimensional damage detection, coastal mapping, photogrammetry, GNSS-R, and deep learning.